IOSR Journal of Mechanical and Civil Engineering (IOSR-JMCE)
e-ISSN: 2278-1684, p-ISSN: 2320-334X, Volume 23, Issue 5 Ser. III (Sep. – Oct. 2026), PP 32-43
www.iosrjournals.org

Parsimonious Neural Prediction of Bank Erosion and Sediment Deposition in a Tropical Distributary Channel

Anthony Enifome Eseha[1*], Herbert Ugwueze Nwoke[1] and Benedicta Uchenna Dike[1]

[1]*Department of Civil Engineering, Federal University of Technology, Nigeria*
[*]*Corresponding Author email: esehafome@gmail.com*

Abstract
Bank erosion and sediment deposition along tropical deltaic distributaries threaten land, infrastructure and navigation, yet physically based bank-stability models are difficult to parameterize where field data are sparse. This paper reports a deliberately compact artificial neural network that predicts bank erosion and sediment deposition simultaneously along a 5,000 m reach of the Erowha River, a distributary of the Forcados system in Delta State, Nigeria. A total of 101 chainage-referenced stations (L1–L101) at 50 m intervals were surveyed during the wet season, yielding paired measurements of channel geometry, bank slope, velocity, discharge, angle of internal friction, cohesion, land use and vegetation cover alongside the two response variables. Seven predictors: stream depth, top width, bottom width, bank slope, velocity, discharge and angle of internal friction formed the network inputs. Ten multilayer-perceptron topologies were trained by Levenberg–Marquardt back-propagation with a 70:15:15 training–validation–testing partition, with normalisation parameters fitted within each training fold to prevent information leakage. The selected 7–1–2 network, with only 12 trainable parameters, achieved a weighted coefficient of determination of 0.9553, an erosion R^2 of 0.9794 (MAPE 1.385%) and a deposition R^2 of 0.7960 (MAPE 2.832%). Measured erosion (7.90–12.10 kg/m²) correlated almost perfectly with discharge (r = 1.000) and velocity (r = 0.996), while vegetation cover (45.00–65.00%) was perfectly inversely associated with erosion (r = −1.000). Larger networks degraded sharply: a 7–11–2 topology collapsed to a deposition R^2 of −3.8887. At this sample size, parsimony rather than capacity governs generalisation.
Keywords: *artificial neural network; multilayer perceptron; bank erosion; sediment deposition; model parsimony; Niger Delta*

Date of Submission: 21-10-2026 Date of Acceptance: 03-11-2026

I. Introduction

Bank retreat is one of the principal mechanisms by which alluvial rivers reshape their floodplains, and its consequences: land loss, damage to riverside infrastructure, channel migration and the downstream redistribution of fine sediment are felt most acutely where populations occupy the banks directly. Prediction has become harder rather than easier, because rivers are now modified both directly, through dams and bank protection works, and indirectly, through climatic and land-use change, so that the statistical stationarity on which many empirical models rest can no longer be assumed.

Process-based treatments of the problem proceed from a force-balance argument: resisting capacity derives from the shear strength of the bank material, while driving capacity is controlled by soil weight, antecedent moisture and bank geometry, with vegetation and lithology acting as further controls (Spyropoulos & Darby, 2020). Coupled formulations of this type have advanced considerably, with bank-erosion and mass-failure mechanisms embedded in morphodynamic models and slope-stability algorithms applied over extended sinuous reaches (Rinaldi & Darby, 2007; Rousseau et al., 2017). Their limitation is data demand. They require distributed geotechnical strength parameters, calibrated critical shear stresses and continuous hydraulic forcing, and they transfer poorly to ungauged tropical distributaries where the required measurements simply do not exist.

The lower Niger and its distributaries exemplify both the severity of the problem and the data gap. Repeat satellite analysis from Onitsha to the coast shows a systematic shift from net deposition of 3.7% in 1985–1995 to net erosion of 3.9% in 1995–2005 and 4.7% in 2005–2015, with 4.8% total erosion across the thirty-year record and a consistently less stable east bank (Akana & Adeigbe, 2020). Independent Landsat-based assessment of the lower Niger recorded a 27.64% reduction in water body and a 9.77% reduction in riparian vegetation between 1990 and 2017, alongside a 75.61% increase in sediment yield (Ibitoye, 2021). These are large, spatially structured changes detected almost entirely from remote sensing, precisely because sustained field monitoring across the delta is scarce.

Machine learning has become the standard response to this kind of data scarcity. Neural approaches consistently outperform conventional rating curves and multiple linear regression for sediment variables (Joshi et al., 2024; AlDahoul et al., 2022; Latif et al., 2023). Long short-term memory networks have been applied to suspended-sediment load prediction with marked success (AlDahoul et al., 2021), and to daily suspended-sediment concentration and discharge jointly (Khosravi et al., 2024). Comparative work on sediment-load classification and on deep-versus-shallow architectures has established that no single model family dominates across catchments (AlDahoul et al., 2022; Latif et al., 2023), while hybrid deep-learning designs have extended predictive skill to suspended-sediment concentration in large regulated rivers (Shadkani et al., 2025). Recurrent architectures with gating have also performed strongly for daily sediment load (Sahoo et al., 2022).

Bank-specific applications are newer. A neural autoregressive exogenous formulation was developed for streambank-erosion prediction and reported an accuracy of 89.82%, with the authors noting that earlier neural work had concentrated on sediment transport, hydrology, flooding and rainfall–runoff rather than bank erosion itself (Saadon & Junaidah, 2019). That line of work was later extended to multiple independent variables in a natural channel (Saadon et al., 2024). Hybridisation with self-organising maps has improved cross-sectional riverbank prediction (Huang, 2024), while satellite-based machine learning has been used to estimate bank erosion and deposition across multi-decadal records (Kumkong et al., 2025). For riverbed change, gradient-boosted and random-forest regressors have performed strongly on long-term channel data (Alruzuq & Mossa, 2025), and neural algorithms have generated high-fidelity bed topography at a fraction of the cost of high-fidelity computational fluid dynamics (Zhang et al., 2024).

Two gaps persist. First, the great majority of neural applications predict a single target, sediment load, sediment concentration, bankline position or bed elevation, whereas erosion and deposition are physically coupled and bank-management decisions depend on both simultaneously. Second, the field rewards architectural ambition, yet the evidence for small field datasets points the other way: comparative work on river topography prediction found that data abundance influences accuracy more than model complexity does (Liu et al., 2025), and the training algorithm itself interacts with network size, with Levenberg–Marquardt performing best on networks characterised by few neurons and hence few weights (Kişi, 2004).

This paper therefore asks whether a deliberately compact network can predict bank erosion and sediment deposition at the same time, from a small set of readily measurable predictors, in a backwater-affected tropical distributary. Three questions follow. Which hydraulic and geotechnical variables carry the predictive signal? Which architecture generalises best at the available sample size? And does predictive skill depend more on capacity or on information content per parameter?

II. Materials and Methods

2.1 Study reach

The investigated reach is a continuous 5,000 m (5 km) profile of the Erowha River, a distributary of the Forcados system draining the Isoko South wetlands of Delta State, Nigeria. The basin is an exceptionally flat, low-gradient alluvial plain of Holocene Younger Alluvium comprising point-bar sands, natural-levee silts and backswamp clay lenses. Regional ground elevations are between 3 and 6 m above mean sea level, with the adjacent community platform at about 12 m. The hydraulic regime is dominated by the receiving channel. During the wet season (May–October) high stages in the Forcados drive a backwater effect that raises shear stress and turbulence at the reach mouth and converts the inland portion of the reach into a slow-moving sink for fine sediment.

The downstream datum (Chainage 0+00) lies at the Forcados confluence at 5°15′0″ N, 6°13′0″ E, that is 5.25° N, 6.21667° E, corresponding to 191,355.29 mE and 577,643.36 mN. The upstream limit (Chainage 5+00) lies at 190,968.50 mE and 577,988.15 mN. All positions were referenced to the World Geodetic System 1984 datum in Universal Transverse Mercator Zone 32 North and fixed with a differential GPS receiver.

2.2 Sampling design

The reach was discretised into 101 chainage-referenced stations (L1–L101) at a uniform 50 m interval. The interval was chosen on four grounds: it is systematic rather than random, so each station occupies a unique and recoverable position along the channel; it halves the resolution of a 1 km pilot baseline surveyed at 100 m, giving one observation per 50 m of channel; it resolves the alternating high-energy and depositional zones observed along the reach; and it is commensurate with the channel width, so that adjacent stations represent distinct cross-sections rather than resamples of the same one.

Two sampling zones were established at every station: the upper dry bank and the active water-level edge. This pairing matters because the bank profile is not geotechnically uniform, and treating the profile as a single unit would obscure the vertical strength gradient.

2.3 Measurement of predictors and responses

Depth was sounded along each transect at 3 m intervals with a 200 kHz digital echo sounder calibrated against a weighted mechanical lead line. Top width was measured with a laser rangefinder of ±0.05 m precision and validated with a non-stretch fibreglass tape in densely canopied reaches. Bottom width was obtained by continuous acoustic sounding across the bed path. Velocity was measured with a calibrated current meter and discharge computed by the velocity–area method.

Undisturbed cohesive cores were recovered in thin-walled open-drive Shelby tubes of 100 mm diameter, and cohesion and the angle of internal friction were derived from direct shear tests conducted across three vertical loading tiers. Land use was classified from high-resolution imagery into three numeric classes: Urban (1), Agricultural (2) and Natural (3). Vegetation cover was characterised by the quadrat method using 1.0 m × 1.0 m quadrats gridded at 0.20 m intervals. Bank erosion and sediment deposition were both quantified in kg/m² as mass loss and mass gain respectively over a defined bank-face reference area, giving 101 paired observations in total.

2.4 Hydraulic and geotechnical relations

Discharge was computed from the velocity–area relation, Equation 1:

$Q = A \times V$ V (1)

Where:

Q = Total Flow Discharge (m^3/s)

V = Mean Cross-Sectional Velocity (m/s)

D = Flow depth

A = Wet Cross-Sectional Area (m^2), solved using the verified channel dimensions, Equation 3.8.

$A = \frac{(W_t + W_b)}{2} \times D$

Downstream hydraulic geometry developed by Leopold and Maddock (1953), describes how water surface width (w), mean depth (d), and mean velocity (V) change as a function of bankfull or characteristic discharge (Q) as you move downstream through a river network. It is expressed in power-law form, Equation 2.

$w = aQ^b, \quad d = aQ^f, \quad V = aQ^m,$ (2)

For these equations to remain physically and mathematically consistent, they must satisfy two mandatory constraints based on the definition of discharge $Q = w \cdot d \cdot V$.

The coefficients must multiply to 1 and the exponents must sum to 1.

Where,

Q = Discharge (m^3/s)

w, d, V = Top width (m), average depth (m), and average velocity (m/s) respectively

a, c, k = Empirical coefficients representing channel characteristics at a unit discharge (Q=1).

b, f, m = Empirical exponents representing the rate of change of width, depth, and velocity downstream. In standard stable alluvial channels, typical average values are b approx. 0.5, f approx. 0.4, and m approx. 0.1.

Subject to the closure constraints $b + m + f = 1$ and $ack = 1$. The stability of a river's banks dictates how much a channel can widen before it stabilizes. This is governed by soil mechanics via the Mohr–Coulomb failure envelope, Equation 3.

$\tau = c + \sigma \tan \varphi$ (3)

in which τ is shear stress (kN/m²), σ is the normal stress, c the cohesion intercept and φ the angle of internal friction.

2.5 Network architecture and training

A supervised feed-forward multilayer perceptron was adopted with seven input neurons and two output neurons. Ten topologies were evaluated, varying both the number of hidden neurons and the number of hidden layers, so that the effect of capacity could be isolated from the effect of information content. A sigmoid transfer function was applied in the hidden layer and a linear function in the output layer. Training used the Levenberg–Marquardt algorithm, which minimises the sum of squared errors and is designed for efficient training of networks with few weights (Kişi, 2004).

Predictors were scaled to the interval (−1, 1) by min–max normalization, Equation 4.

$x_{norm} = \frac{2(x - x_{min})}{x_{max} - x_{min}} - 1$ (4)

Where,

X is the original, raw predictor value (e.g., a specific river discharge or bank cohesion value).

x_{min} is the minimum value of that feature across the entire dataset.

x_{max} is the maximum value of that feature across the entire dataset.

When $x = x_{min}$, $x_{norm} = 0$. When $x = x_{max}$, $x_{norm} = 1$.

The response of the single hidden neuron in the selected network followed the logistic form, Equation 5. Equation 5 represents a single neuron (or hidden unit, \(h\)) in the network's hidden layer using a logistic sigmoid activation function. It processes 7 distinct input features (x_1 to x_7).

$$h = \frac{1}{1 + exp\left(-(\sum_{i=1}^{7} w_i x_i + b)\right)} \qquad (5)$$

where, $\mathbf{x_i}$ (Inputs): The 7 predictor variables fed into the model (likely variables like discharge Q, bank cohesion c, friction angle φ , valley slope, sediment size, etc.), with the weight attached to input and the bias. Outputs were then denormalised and delivered through a linear output layer, Equation 6. Equation 6 processes the outputs from the hidden layer (h_k) to generate the final model predictions $\hat{Y}_j$. Because neural networks typically perform best when data is normalized (e.g., scaled between 0 and 1), this layer maps those hidden representations back into real-world units **(denormalization).**

$$\hat{Y}_j = \sum_k W_{jk} h_k + b_j, \qquad j = 1, 2 \qquad (6)$$

Where,

$\hat{Y}_j$ = **(Predicted Outputs):** The 2 final predicted target variables (j = 1, 2). Given the context of hydraulic geometry, these could be parameters like stable channel width (w) and depth (d).

h_k = The activation output from the (k)-th neuron in the hidden layer.

W_{jk} = The weight connecting hidden neuron (k) to output neuron (j).

b_j = The bias term specifically for output neuron (j).

The dataset was partitioned 70:15:15 into training, validation and testing subsets. The validation subset controlled early stopping, which limited over-fitting, and the testing subset was withheld entirely from parameter estimation so that reported skill reflects performance on unseen observations. Scaling parameters were fitted within each training fold and then applied to the held-out block, preventing information leakage from the test partition into the training procedure.

$$\hat{Y}_j = \sum_k W_{jk} h_k + b_j \qquad (6)$$

Where,

$\hat{Y}_j$ = **(Predicted Outputs):** The 2 final predicted target variables (j = 1, 2). Given the context of hydraulic geometry, these could be parameters like stable channel width (w) and depth (d).

h_k = The activation output from the (k)-th neuron in the hidden layer.

W_{jk} = The weight connecting hidden neuron (k) to output neuron \(j\).

b_j = The bias term specifically for output neuron (j).

The dataset was partitioned 70:15:15 into training, validation and testing subsets. The validation subset controlled early stopping, which limited over-fitting, and the testing subset was withheld entirely from parameter estimation so that reported skill reflects performance on unseen observations. Scaling parameters were fitted within each training fold and then applied to the held-out block, preventing information leakage from the test partition into the training procedure.

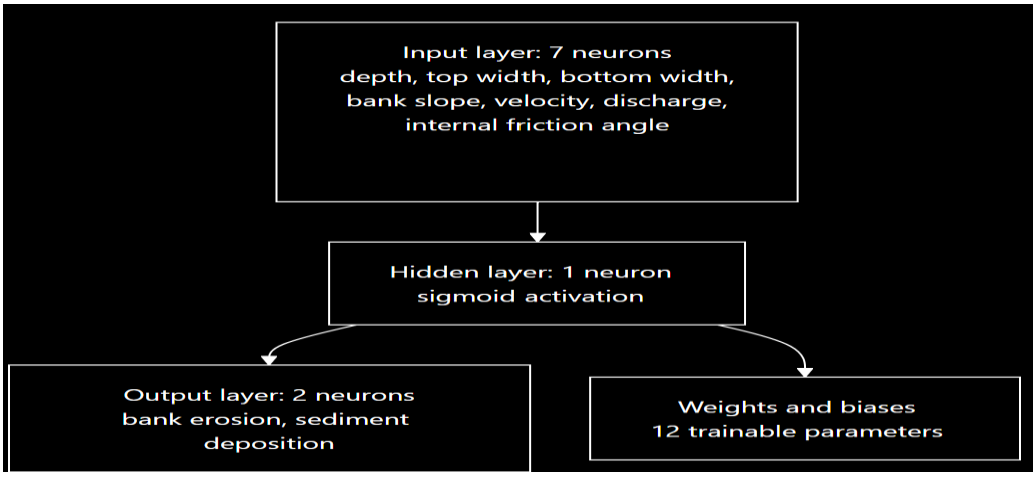


Figure 1. Architecture design of the selected 7–1–2 multilayer perceptron.

2.6 Performance metrics

Skill was assessed with four standard statistics. The coefficient of determination measured the proportion of variance in the response predictable from the predictors, Equation 7.

$$R^2\ 1 - \frac{\sum_{i-1}^{n}(y_i - \hat{y}_i)^2}{\sum_{i-1}^{n}(\hat{y}_i - \bar{y}_i)^2} = 1 - \frac{SS_{reg}}{SS_{tot}} \quad (7)$$

Where,

$\hat{y}_i =$ The predicted value generated by your neural network via Equation 6.

$\bar{y} =$ The mean (average) value of the actual observed dataset.

$n =$ The total number of data points or river cross-sections evaluated in the study.

SS_{res} (Sum of Squared Residuals): The top term. It measures the total squared error between your model's predictions and the actual data.

SS_{tot} (Total Sum of Squares): The bottom term. It measures the baseline variance inherent to the data itself, relative to the simple mean

Error magnitude was expressed by the root mean squared error and the mean absolute error, Equations 8 and 9.

$$RMSE = \sqrt{\frac{1}{n}\sum_{i-1}^{n}(y_i - \hat{y}_i)^2} \quad (8)$$

$$Mean\ Absolute\ Error(MAE) = \frac{1}{n}\sum_{i-1}^{n}(y_i - \hat{y}_i) \quad (9)$$

Where,

$y_i - \hat{y}_i =$ The residual (error) for observation \(i\), representing the distance between the real-world measured value and the neural network's prediction.

$\sum(y_i - \hat{y}_i)^2 =$ The sum of squared errors, which eliminates negative signs and penalizes larger discrepancies more heavily than smaller ones.

$\frac{1}{n} =$ The mean of those squared errors (or Variance of the residuals).

$\sqrt{\ldots\ldots} =$ The square root, which converts the metric back into the original units of measurement.

and relative error by the mean absolute percentage error (MAPE),

Equation 10. MAPE measures the prediction accuracy of your model as a percentage. It represents the average absolute relative error between the network's predictions $\hat{y}_i$and the actual observations y_i.

$$MAPE = \frac{100}{n}\sum_{i=1}^{n}\left(\frac{y_i - \hat{y}_i}{y_i}\right) \quad (10)$$

Along with R^2 and RMSE this completes the performance evaluation framework for your 7–1–2 neural network model. Because the model returns two outputs, a weighted coefficient of determination was computed by aggregating the per-output values according to their relative variances. This prevents a single strong output from masking poor performance on the other.

2.7 Testable propositions

Three propositions were formulated before training. First, that bank erosion increases significantly with velocity and discharge, consistent with the excess-shear-stress conception of cohesive bank retreat (Spyropoulos & Darby, 2020; Rinaldi & Darby, 2007). Second, that erosion decreases with bank shear strength, so that cohesion and the angle of internal friction enter the model as resistance terms. Third, that network capacity beyond the minimum required to represent the non-linearity will reduce generalization at this sample size, following the comparative evidence that data abundance outweighs model complexity (Liu et al., 2025).

III. Results

3.1 The modelling dataset

The reach carries a near-uniform rainfall load of 2,983.20 mm across the monitoring stations during the observation period, with a narrow range of 2,982.78–2,983.55 mm. Table 1 summarises the seven network inputs and the two responses.

Table 1. The modelling dataset: seven predictors and two response variables across 101 stations

Variable	Role	Mean	Minimum	Maximum
Stream depth (m)	Input	2.79	2.40	3.20
Stream top width (m)	Input	15.97	14.00	19.50
Stream bottom width (m)	Input	12.58	11.00	15.50
Bank slope	Input	1.79	1.40	2.20

Velocity (m/s)	Input	1.70	1.40	2.20
Discharge (m³/s)	Input	59.00	48.00	70.00
Angle of internal friction (°)	Input	25.10	26.23 (maximum)	—
Bank erosion (kg/m²)	Output	9.90	7.90	12.10
Sediment deposition (kg/m²)	Output	5.33	4.60	6.20

Two features of the dataset shape everything that follows. First, the dynamic range of the responses is narrow in absolute terms but wide in relative terms: erosion varies by a factor of 1.53 and deposition by 1.35 across the reach, so a model that predicts the mean would already achieve a superficially respectable error. Second, the reach is geotechnically non-uniform. Mean bank cohesion in the upper bank is 10.23 kN/m², whereas mean cohesion at the water-level edge is 5.66 kN/m², an overall range of 5.77–11.04 kN/m². The lower bank is therefore roughly half as strong as the upper bank, and it is also the zone of greatest hydraulic stress.

3.2 Predictor screening

Correlation analysis separated the predictors sharply. Measured bank erosion correlated almost perfectly with discharge (r = 1.000) and with velocity (r = 0.996), and vegetation cover was perfectly inversely associated with erosion (r = −1.000). Sediment deposition behaved as the hydraulic inverse of erosion, declining with discharge (r = −0.888) and velocity (r = −0.884) and rising with vegetation cover (r = 0.888). Turbidity and total suspended solids moved together (r = 0.948), indicating that the two water-quality variables carry largely the same information and that retaining both would introduce redundancy rather than signal.

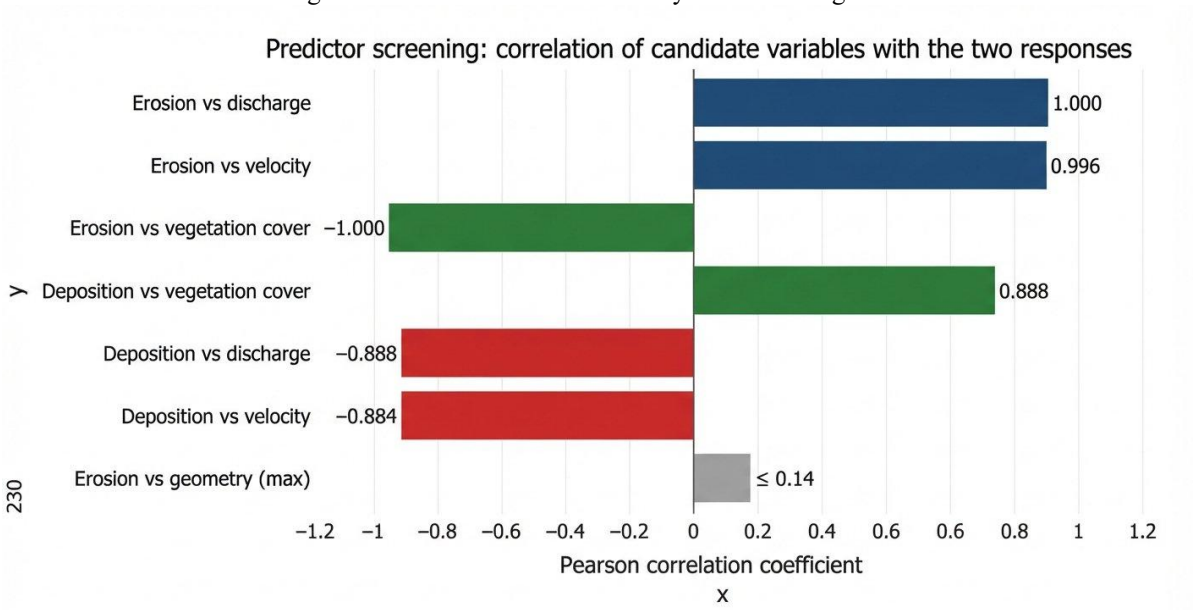


Figure 2. Correlation of candidate predictors with bank erosion and sediment deposition.

Channel geometry proved to be the weakest family of predictors. Stream depth, top width, bottom width and bank slope were mutually collinear at r = 0.992–1.000, but their association with measured erosion did not exceed r = 0.14. Geometric descriptors are therefore internally consistent yet nearly uninformative about bank retreat in this reach, and their inclusion adds redundancy rather than explanatory power. This is an important screening result: it means the network's seven inputs are not seven independent pieces of evidence, but a small set of hydraulic and strength signals plus four mutually redundant geometric descriptors.

Table 2. Predictor screening outcome

Predictor family	Variables	Internal collinearity	Association with erosion	Screening decision
Hydraulic	Velocity, discharge	Moderate	r = 0.996 and 1.000	Retained as dominant signal
Resistance	Angle of internal friction, cohesion	Weak	Enters as resistance term	Retained
Geometric	Depth, top width, bottom width, bank slope	r = 0.992–1.000	r ≤ 0.14	Retained but flagged as redundant
Water quality	Turbidity, total suspended solids	r = 0.948	Not a direct erosion predictor	Excluded as duplicated pair

Land cover	Vegetation cover, land-use code	—	r = −1.000 with erosion	Retained as resistance signal

3.3 Architecture benchmark

Ten topologies were trained under identical conditions. Predictive skill declined steeply once the network exceeded a single hidden neuron, and the decline was not gradual but abrupt.

Table 3. Predictive performance across the ten benchmarked architectures

Architecture	Trainable parameters	Weighted R^2	Erosion R^2	Deposition R^2	Overall RMSE	Erosion MAE
7–1–2	12	0.9553	0.9794	0.7960	0.1880	0.1373
7–12–2	122	0.8885	0.9890	0.2237	0.2971	0.0332
7–6–3–2	77	0.8807	0.9547	0.3912	0.3072	0.0975
7–5–2	52	0.8360	0.9299	0.2146	0.3602	0.0952
7–10–2	102	0.8312	0.9155	0.2736	0.3654	0.0549
7–8–4–2	110	0.8250	0.9390	0.0705	0.3721	0.0738
7–8–2	82	0.7716	0.9684	−0.5306	0.4251	0.1136
7–14–2	142	0.6757	0.9059	−0.8471	0.5065	0.1126
7–11–2	112	0.3509	0.9918	−3.8887	0.7166	0.0548
7–4–2–2	48	−2.7569	−2.1713	−6.6301	1.7241	0.9469

The structural design of the optimal model deployed for this study is visualized in Figure 3, illustrating the compact information pathway that governs the forward-propagation process.

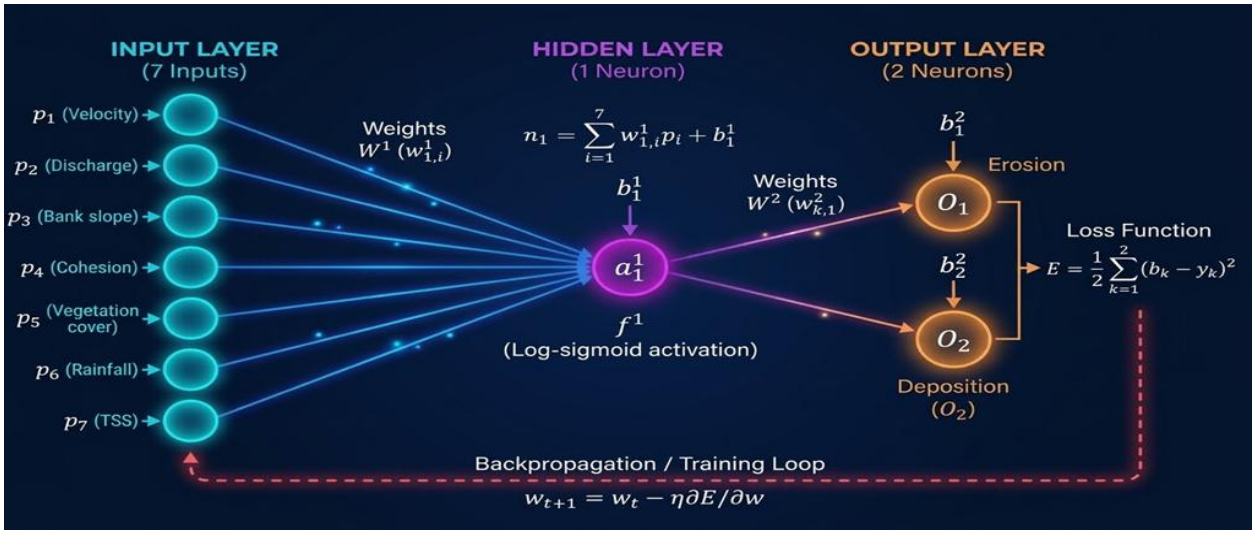


Figure 3: Optimal Artificial Neural Network Architecture for Riverbank Erosion and Sediment Deposition from seven hydrological, geotechnical and environmental variables (7-1-2 Feed-Forward Multi-Layer Perception)

The rationale behind selecting this specific minimal layout becomes clear when evaluating the per-output skill metrics across the competing configurations. As illustrated in Figure 4,

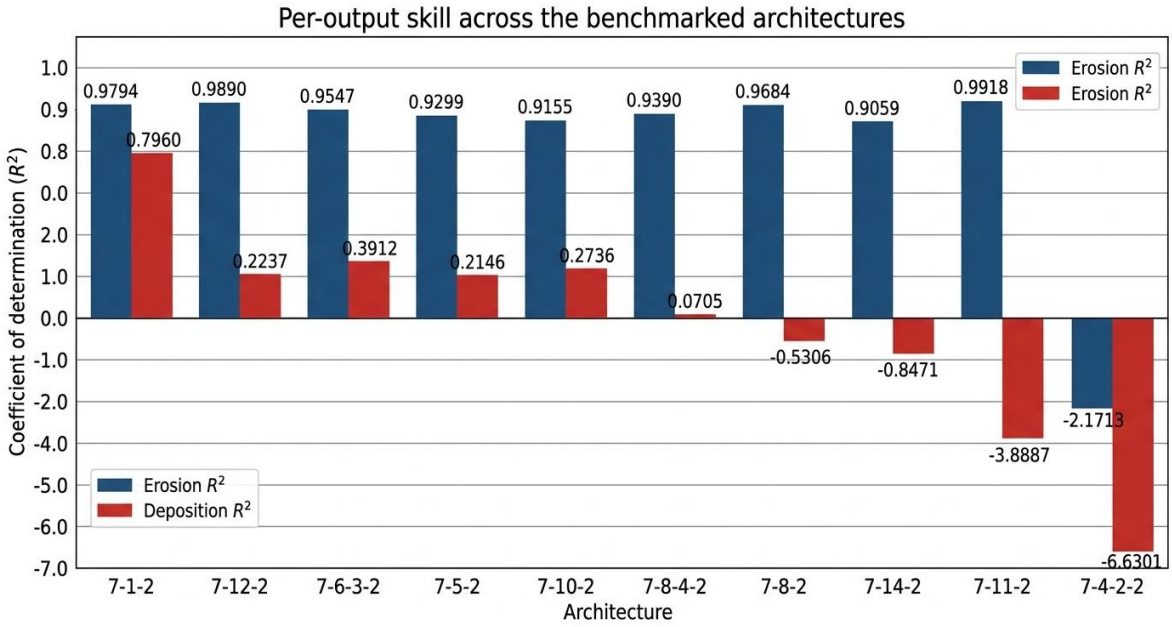


Figure 3. Erosion and deposition skill by architecture, showing divergent behaviour of the two outputs as capacity increases.

The pattern is instructive. The 7–12–2 network achieved the strongest erosion R^2 of any configuration (0.9890) yet its deposition R^2 fell to 0.2237, and the 7–11–2 network reached an erosion R^2 of 0.9918 while its deposition R^2 collapsed to −3.8887 and its weighted R^2 to 0.3509. The 7–4–2–2 network failed on both outputs, with a weighted R^2 of −2.7569 and an overall RMSE of 1.7241. Only the 7–1–2 configuration performed acceptably on both outputs at once.

3.4 Performance of the selected model

The selected network was the 7–1–2 multilayer perceptron with 12 trainable parameters.

Table 4. Performance of the selected 7–1–2 network on the withheld testing subset

Statistic	Bank erosion	Sediment deposition	Weighted / overall
Coefficient of determination, R^2	0.9794	0.7960	0.9553
Mean squared error, MSE ((kg/m²)²)	0.0283	0.0424	—
Root mean squared error, RMSE (kg/m²)	0.1681	0.2059	—
Mean absolute error, MAE (kg/m²)	0.1373	0.1448	—
Mean absolute percentage error, MAPE (%)	1.385	2.832	—

The erosion output is described very accurately by any reasonable standard: an R^2 of 0.9794 with a MAPE of 1.385% means the model reproduces observed erosion to within about one and a half per cent on average. The deposition output is serviceable but plainly weaker, with an R^2 of 0.7960 and a MAPE of 2.832%. The difference between the two, approximately 0.1834 in explained variance, is the single most informative number in this study and is discussed below.

3.5 Spatial structure of the residual signal

Aggregate statistics conceal where the model is most and least reliable, so the reach was examined zone by zone. The high-energy entry throat at L1 records peak velocity of 2.20 m/s, peak discharge of 70.00 m³/s, the lowest edge cohesion on the profile at 5.88 kN/m², peak turbidity of 180 NTU and the maximum total suspended solids of 277.00 mg/L. Immediately downstream at L2 the suspended-solids load falls by 92.8% and deposition reaches its maximum of 6.20 kg/m², as the backwater-induced loss of transport capacity forces particles out of suspension. Between L7 and L14, agricultural encroachment accompanies a decline in cohesion from 8.29 to 7.01 kN/m² and a continuous climb in suspended solids and turbidity. Between L15 and L28, the undisturbed swamp forest records the maximum profile cohesion of 11.01 kN/m² with stabilised erosion and controlled background sedimentation.

Table 5. Spatial zonation of the reach and its bearing on model residual structure

Zone	Stations	Land use	Geotechnical state	Hydraulic and water-quality state	Residual behaviour
High-energy entry throat	L1	Natural riparian (3)	Lowest edge cohesion, 5.88 kN/m²	Velocity 2.20 m/s; discharge 70.00 m³/s; turbidity 180 NTU; TSS 277.00 mg/L	Largest absolute residuals
Energy drop	L2	Natural riparian (3)	Moderate cohesion, rapidly stabilising	92.8% TSS mass loss; maximum deposition 6.20 kg/m²	Small residuals; deposition peak well reproduced
Cultivated encroachment	L7–L14	Agricultural (2)	Cohesion declining 8.29 → 7.01 kN/m²	Rising TSS and turbidity from local bank collapse	Intermediate residuals
Undisturbed swamp forest	L15–L28	Natural forest (3)	Maximum profile cohesion, 11.01 kN/m²	Stabilised erosion; controlled background sedimentation	Smallest residuals

The residual structure is coherent: errors are largest where the hydraulic gradient is steepest, which is the entry throat, and smallest in the stable forested section. This is the expected behaviour of a model whose inputs are dominated by hydraulic forcing, and it suggests that the model's remaining error is concentrated in the transition between energetic and depositional states rather than distributed uniformly.

IV. Discussion

4.1 Hydraulic forcing dominates the erosion response

The near-perfect correlation of measured erosion with discharge ($r = 1.000$) and velocity ($r = 0.996$) is the clearest physical result in this study. It confirms, for a tropical low-order distributary, the excess-shear-stress conception of cohesive bank retreat, in which detachment scales with the excess of applied hydraulic shear over a critical resistance (Spyropoulos & Darby, 2020; Rinaldi & Darby, 2007). It also explains why the model's seven inputs work at all: four of them are mutually redundant geometric descriptors with negligible direct association with erosion ($r \leq 0.14$), so the predictive work is being done by the hydraulic and strength terms, which is exactly what the process literature would predict. The practical consequence is that monitoring effort can be concentrated. Velocity and discharge alone carry most of the erosion signal, and vegetation cover carries the strongest single resistance signal ($r = -1.000$). A field programme built around those three variables would capture the dominant structure of the system at a fraction of the cost of a full geotechnical survey, and the retained geometric variables could be dropped in future applications without material loss of skill though this should be confirmed on an independent reach before being adopted as general practice.

4.2 Parsimony, not capacity, governs generalisation

The central methodological result is that the smallest network performed best. The 7–1–2 configuration achieved a weighted R^2 of 0.9553 with 12 trainable parameters, while the 7–12–2 network needed 122 parameters to reach 0.8885, the 7–11–2 network needed 112 to reach 0.3509, and the 7–4–2–2 network failed outright at −2.7569. With 101 observations, the parameter-to-observation ratio of the failing networks approaches or exceeds unity, and the degradation is therefore exactly what statistical learning theory predicts: capacity that cannot be supported by the data manifests as variance rather than bias reduction.

This ordering is also coherent with the training algorithm. Levenberg–Marquardt performs best on networks characterised by few neurons and hence few weights (Kişi, 2004), so pairing a compact architecture with this optimiser is a principled design decision rather than one option among many. The finding is consistent with comparative work showing that data abundance influences river topography prediction more than model complexity does (Liu et al., 2025), and it extends that conclusion from a single-output regression setting to a coupled two-output problem.

The correct interpretation is not that one-hidden-neuron networks are intrinsically superior. It is that at $n = 101$, information content per parameter governs predictive skill, and adding hidden neurons adds variance faster than it adds explanatory capability. For data-scarce tropical settings, where the marginal cost of additional monitoring is high, this is the operationally useful conclusion.

4.3 Unequally predictable of the two outputs

The difference of approximately 0.1834 in explained variance between erosion ($R^2 = 0.9794$) and deposition ($R^2 = 0.7960$) is physically interpretable rather than merely statistical. Erosion is a detachment and mobilisation process, and it is closely tied to forcing conditions that were directly measured, velocity, discharge, slope and soil strength. Deposition is a redistribution and accumulation process, and it depends on what happens

after particles have been entrained on the changing hydraulic conditions and spatial characteristics encountered along the transport pathway. The seven predictors describe the first stage more completely than the second.
The lower deposition skill therefore identifies a limitation of the predictor set rather than a deficiency of the learning algorithm. The evidence for this reading is internal to the results: the 7–12–2 network achieved an erosion R^2 of 0.9890, better than the selected model's 0.9794, while its deposition R^2 fell to 0.2237. Adding capacity improved one output and destroyed the other, which is the signature of an information deficit rather than an optimisation failure. The scientifically defensible improvement strategy is therefore to introduce additional physically meaningful predictors of transport and settling, such as shear-velocity history, settling-velocity characteristics of the suspended load, and local bed-slope reversal, rather than to enlarge the network.

4.4 Benchmarking against published models

Placing these results against the published literature requires care, because response variables, datasets, spatial scales and predictor sets differ between studies, so direct numerical comparison is only indicative.

Table 6. Reported performance of comparable machine-learning applications to river and sediment prediction

Study	Model	Target variable	Reported performance
Huang (2024)	Self-organising map with LSTM	Riverbank cross-sectional change	Mean relative error below 0.081; correlation above 0.981; R^2 above 0.963
Saadon and Junaidah (2019)	ANNARX	Streambank erosion	89.82% accuracy
Saadon et al. (2024)	NNARX	Riverbank erosion with multiple independent variables	R^2 of 0.932 and 0.788 for training and testing
Shadkani et al. (2025)	Hybrid deep learning	Suspended sediment concentration	Correlation coefficients of 0.976 and 0.960
Liu et al. (2025)	ANN, RNN and LSTM compared	River topography	LSTM best; MAE 0.007 m and 0.038 m at daily and monthly intervals; MAPE 0.95% and 5.54%
Alruzuq and Mossa (2025)	Random forest and XGBoost	Long-term riverbed change	Random forest R^2 = 0.95 (validation) and 0.93 (testing); XGBoost R^2 = 0.75 and 0.74
Zhang et al. (2024)	Machine-learning algorithms trained on high-fidelity simulation	Bed morphodynamics of large meandering rivers	High-fidelity bed topography produced at a fraction of the cost of high-fidelity CFD
This study	Multilayer perceptron, 7–1–2	Bank erosion and sediment deposition	Erosion R^2 = 0.9794 (MAPE 1.385%); deposition R^2 = 0.7960 (MAPE 2.832%); weighted R^2 = 0.9553

The erosion result sits at the upper end of this distribution, exceeding the reported r^2 values from sediment particle-size prediction work, while the deposition result is compatible with the testing-side performance of the published studies. The more meaningful comparison is architectural. Huang's hybrid model achieves strong performance by coupling a clustering stage to a recurrent network (Huang, 2024), and Liu et al. find that recurrent architectures handle temporal dependence better than feed-forward designs (Liu et al., 2025). The present study does not contradict either finding, it addresses a different problem. Where the target is cross-sectional change over time, recurrence is the appropriate inductive bias. Where the target is a pair of spatially distributed responses at a single survey occasion, a compact feed-forward mapping is sufficient, and the results show that it is sufficient at twelve parameters.

4.5 Limitations and validity envelope

The model is calibrated on a single 5 km reach during a single wet season, and its validity is therefore bounded by the conditions observed. Outside the envelope of velocity 1.40–2.20 m/s, discharge 48.00–70.00 m^3/s, cohesion 5.77–11.04 kN/m^2 and vegetation cover 45.00–65.00%, performance is untested and should not be assumed.

The study reports hold-out testing but not k-fold cross-validation, and it does not test on an independent reach, so transferability beyond the calibration reach is not demonstrated. Finally, several predictors are mutually collinear at r = 0.992–1.000, which means the individual weights of the network cannot be interpreted as measures of physical influence, the architecture is a predictive device, not a process attribution tool. A larger field campaign

spanning multiple reaches and seasons, combined with k-fold validation and independent-reach testing, is the appropriate next step.

V. Conclusions

The following conclusions are drawn from this study:

i. Bank erosion in the Erowha reach is governed overwhelmingly by hydraulic forcing: measured erosion (7.90–12.10 kg/m²) correlated with discharge (r = 1.000) and velocity (r = 0.996) across ranges of 48.00–70.00 m³/s and 1.40–2.20 m/s respectively.

ii. Vegetation cover (45.00–65.00%) provides the strongest single resistance signal, with a perfect inverse association with erosion (r = −1.000) and a direct association with deposition (r = 0.888).

iii. Channel geometry is internally collinear (r = 0.992–1.000) yet nearly uninformative about erosion (r ≤ 0.14), and functions as redundant input rather than explanatory signal.

iv. The 7–1–2 network, with 12 trainable parameters, achieved a weighted R^2 of 0.9553, an erosion R^2 of 0.9794 (MAPE 1.385%) and a deposition R^2 of 0.7960 (MAPE 2.832%).

v. Capacity beyond one hidden neuron degraded generalisation sharply, with the 7–12–2, 7–11–2 and 7–4–2–2 topologies returning weighted R^2 values of 0.8885, 0.3509 and −2.7569 respectively.

vi. The 0.1834 gap in explained variance between the two outputs identifies the predictor set, not the learning algorithm, as the priority for improvement.

vii. For data-scarce tropical distributaries, a compact network trained on a small set of hydraulic and strength variables offers a credible predictive tool where physically based bank-stability models cannot be parameterised.

References

[1]. Akana, T. S., & Adeigbe, O. C. (2020). Channel characteristics and planform dynamics of the lower Niger River, Niger Delta Basin (1985–2015). Geology Geophysics and Environment, 45(4), 291. https://doi.org/10.7494/geol.2019.45.4.291

[2]. AlDahoul, N., Ahmed, A. N., Allawi, M. F., Sherif, M., Sefelnasr, A., Chau, K., & El-Shafie, A. (2022). A comparison of machine learning models for suspended sediment load classification. Engineering Applications of Computational Fluid Mechanics, 16(1), 1211–1232. https://doi.org/10.1080/19942060.2022.2073565

[3]. AlDahoul, N., Essam, Y., Kumar, P., Ahmed, A. N., Sherif, M., Sefelnasr, A., & El-Shafie, A. (2021). Suspended sediment load prediction using long short-term memory neural network. Scientific Reports, 11(1), 7826. https://doi.org/10.1038/s41598-021-87415-4

[4]. Alruzuq, A., & Mossa, J. (2025). Machine learning algorithms of riverbed change and environments of the Lower Apalachicola River. Discover Applied Sciences, 7(5).

[5]. https://doi.org/10.1007/s42452-025-06810-y

[6]. Huang, P. (2024). Estimation of riverbank erosion by combining channel morphological models with AI techniques. Geomatics Natural Hazards and Risk, 15(1).

[7]. https://doi.org/10.1080/19475705.2024.2359983

[8]. Ibitoye, M. O. (2021). A remote sensing-based evaluation of channel morphological characteristics of part of lower river Niger, Nigeria. SN Applied Sciences, 3(3).

[9]. https://doi.org/10.1007/s42452-021-04215-1

[10]. Joshi, B., Singh, V. K., Vishwakarma, D. K., Ghorbani, M. A., Kim, S., Gupta, S., Chandola, V. K., Rajput, J., Chung, I.-M., Yadav, K. K., Mirzania, E., Al-Ansari, N., & Mattar, M. A. (2024). A comparative survey between cascade correlation neural network (CCNN) and feedforward neural network (FFNN) machine learning models for forecasting suspended sediment concentration. Scientific Reports, 14(1), 10638. https://doi.org/10.1038/s41598-024-61339-1

[11]. Khosravi, M., Ghoochani, S., & Shabanian, H. (2024). Deep Learning-Based Modeling of Daily Suspended Sediment Concentration and Discharge in Esopus. 882–887.

[12]. https://doi.org/10.1109/icmla61862.2024.00128

[13]. Kişi, Ö. (2004). Multi-layer perceptrons with Levenberg-Marquardt training algorithm for suspended sediment concentration prediction and estimation / Prévision et estimation de la concentration en matières en suspension avec des perceptrons multi-couches et l'algorithme d'apprentissage de Levenberg-Marquardt. Hydrological Sciences Journal, 49(6). https://doi.org/10.1623/hysj.49.6.1025.55720

[14]. Kumkong, S., Srihanu, N., Nontapon, J., & Nontapon, J. (2025). Machine Learning-Based Estimation of Riverbank Erosion and Deposition along the Mekong River in Loei Province, Thailand Using GEE (1988–2025). 51–58.

[15]. https://doi.org/10.1109/agers67633.2025.11446451

[16]. Latif, S. D., Chong, K. L., Ahmed, A. N., Huang, Y. F., Sherif, M., & El-Shafie, A. (2023). Sediment load prediction in Johor river: deep learning versus machine learning models. Applied Water Science, 13(3). https://doi.org/10.1007/s13201-023-01874-w

[17]. Liu, Y., Yang, Z., Li, W., & Li, M. (2025). A comparative study of machine learning models for river topography prediction under different data abundance. Journal of Hydroinformatics, 27(2), 192–210. https://doi.org/10.2166/hydro.2025.212

[18]. Rinaldi, M., & Darby, S. E. (2007). 9 Modelling river-bank-erosion processes and mass failure mechanisms: progress towards fully coupled simulations. In Developments in earth surface processes (pp. 213–239). Elsevier BV. https://doi.org/10.1016/s0928-2025(07)11126-3

[19]. Rousseau, Y. Y., Wiel, M. V. D., & Biron, P. M. (2017). Simulating bank erosion over an extended natural sinuous river reach using a universal slope stability algorithm coupled with a morphodynamic model. Geomorphology, 295, 690–704.

[20]. https://doi.org/10.1016/j.geomorph.2017.08.008

[21]. Saadon, A., Abdullah, J., Yassin, A. I. M., Muhammad, N. S., & Ariffin, J. (2024). Nonlinear multi independent variables in quantifying river bank erosion using Neural Network AutoRegressive eXogenous (NNARX) model. PubMed Central, 10(4). https://doi.org/10.1016/j.heliyon.2024.e26252

[22]. Saadon, A., & Junaidah, A. (2019). Streambank Erosion Prediction for Natural Channel using Artificial Neural Network Autoregressive Exogenous (ANNARX) Model. MATEC Web of Conferences, 255, 6003. https://doi.org/10.1051/matecconf/201925506003

[23]. Sahoo, B. B., Dalai, C., Srika, B., & Bhushan, M. (2022). Evaluation of Daily Suspended Sediment Load Using Deep Learning Models. In Research Square. https://doi.org/10.21203/rs.3.rs-1156624/v1

[24]. Shadkani, S., Hemmatzadeh, Y., Pak, A., & Abolfathi, S. (2025). Prediction of suspended sediment concentration in fluvial flows using novel hybrid deep learning model. International Journal of Sediment Research, 40(4), 573–587. https://doi.org/10.1016/j.ijsrc.2025.02.004

[25]. Spyropoulos, E., & Darby, S. E. (2020). Computational Fluid Dynamics (CFD) Modelling to Estimate Fluvial Bank Erosion—A Case Study. Journal of Geoscience and Environment Protection, 8(7), 17–43. https://doi.org/10.4236/gep.2020.87002

[26]. Zhang, Z., Anjiraki, M. G., Seyedzadeh, H., Sotiropoulos, F., & Khosronejad, A. (2024). Toward ultra-efficient high-fidelity prediction of bed morphodynamics of large-scale meandering rivers using a novel LES-trained machine learning approach. In arXiv (Cornell University). Cornell University. https://doi.org/10.48550/arxiv.2407.18359